ADVANCED FUNCTIONAL MATERIALS
www.afm-journal.de

Mechanistic Investigation into Dynamic Function of Third Component Incorporated in Ternary Near-Infrared Nonfullerene Organic Solar Cells

Zhuoyan Wang, Jingjing Ji, Weihua Lin, Yao Yao, Kaibo Zheng, and Ziqi Liang**

Organic solar cells (OSCs) consisting of an ultralow-bandgap nonfullerene acceptor (NFA) with an optical absorption edge that extends to the near-infrared (NIR) region are of vital interest to semitransparent and tandem devices. However, huge energy-loss related to inefficient charge dissociation hinders their further development. The critical issues of charge separation as exemplified in NIR-NFA OSCs based on the paradigm blend of PTB7–Th donor (D) and IEICO–4F acceptor (A) are revealed here. These studies corroborate efficient charge transfer between D and A, accompanied by geminate recombination of photo-excited charge carriers. Two key factors restricting charge separation are unveiled as the connection discontinuity of individual phases in the blend and long-lived interfacial charge-transfer states (CTS). By incorporation of a third-component of benchmark ITIC or $PC_{71}BM$ with various molar ratios, these two issues are well-resolved accordingly, yet in distinctly influencing mechanisms. ITIC molecules modulate film morphology to create more continuous paths for charge transportation, whereas $PC_{71}BM$ diminishes CTS and enhances electron transfer at the D/A interfaces. Consequently, the optimal untreated ternary OSCs comprising 0.3 wt% ITIC and 0.1 wt% $PC_{71}BM$ in the blend deliver higher J_{SC} values of 21.9 and 25.4 mA cm^{-2}, and hence increased PCE of 10.2% and 10.6%, respectively.

1. Introduction

Bulk-heterojunction organic solar cells (OSCs) have been considered as a promising solar energy conversion system because of their light weight, mechanical flexibility, solution-processability as well as the capability of large-scale manufacturing.[1–7] The conventional OSCs comprise of binary donor and acceptor materials, the latter of which can be categorized into either fullerene acceptors (FAs) or nonfullerene acceptors (NFAs). FAs have been well-established while NFAs are in early nourishment yet have demonstrated a brighter prospect than FA analogues due to their diverse chemical structures tunable energy levels as well as the realization of efficient charge transfer between NFA and donor.[8–15] Of particular interest are those ultralow-bandgap ($E_g \leq \approx 1.25$ eV) NFAs with an optical absorption edge that extends to the near-infrared (NIR) region (i.e., 750–1000 nm). When combining these NIR-NFAs with wide-E_g polymer donor, a broader and complementary range of light absorption can be reached, which largely benefit photovoltaic performance.[8,16,17]

However, the low short-circuit current density (J_{SC}) and open-circuit voltage (V_{OC}) are the two hurdles in the NIR-based systems, both of which are intrinsically correlated to the inefficient interfacial charge dissociation.[18] In a binary blend composed of a medium-E_g polymer donor and a NIR-NFA, there usually exists a larger energy offset of lowest unoccupied molecular orbitals (LUMO) levels, which results in the tighter gap between the donor HOMO (i.e., highest occupied molecular orbital) and the acceptor LUMO energy levels. This would facilitate interfacial geminate recombination, giving rise to a potential large voltage loss. On the other hand, in the state-of-art NIR-NFA based OSCs containing 2-((Z)-2-((5-(7-(5-(((1Z,2Z)-1-(cyano(isocyano)methylene)-5,6-difluoro-3-oxo-1,3-dihydro-2H-inden-2-ylidene)methyl)-3-((2-ethylhexyl)oxy)thiophen-2-yl)-4,4,9,9-tetrakis(4-hexylphenyl)-4,9-dihydro-s-indaceno[1,2-b:5,6-b′]dithiophen-2-yl)-4-((2-ethylhexyl)oxy)thiophen-2-yl)methylene)-5,6-difluoro-3-oxo-2,3-dihydro-1H-inden-1-ylidene)malononitrile (IEICO-4F) acceptor,[19] severe charge recombination remains due to the well-miscibility of polymer donor and acceptor, which retard

Z. Wang, J. Ji, Prof. Z. Liang
Department of Materials Science
Fudan University
Shanghai 200433, China
E-mail: zqliang@fudan.edu.cn
W. Lin, Dr. K. Zheng
Department of Chemical Physics and NanoLund
Lund University
P.O. Box 124, Lund 22100, Sweden
Dr. Y. Yao
Department of Physics and State Key Laboratory of Luminescent Materials and Devices
South China University of Technology
Guangzhou 510640, China
Prof. K. Zheng
Department of Chemistry
Technical University of Denmark
Kongens Lyngby DK-2800, Denmark
E-mail: kzheng@kemi.dtu.dk
The ORCID identification number(s) for the author(s) of this article can be found under https://doi.org/10.1002/adfm.202001564.

DOI: 10.1002/adfm.202001564

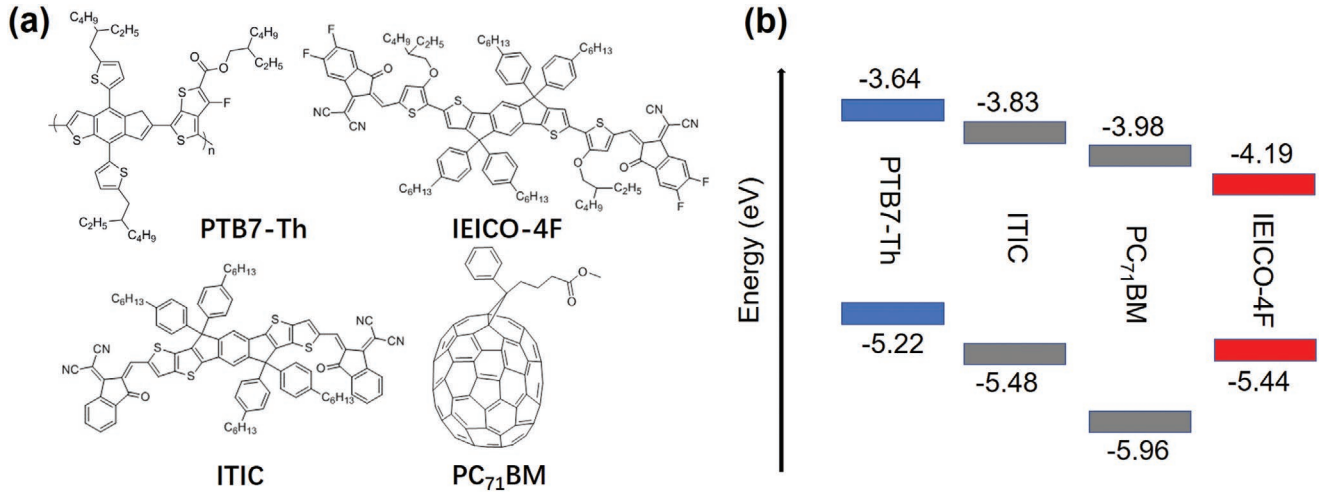

Figure 1. a) Chemical structures of PTB7–Th, IEICO–4F, ITIC, and $PC_{71}BM$ and b) their schematic energy diagrams.

phase segregation for efficient charge separation and transportation. To resolve the above two issues with regard to interfacial charge separation affected by larger offsets of both HOMO and LUMO energy levels in NIR-NFA OSCs, the formation of fine blend film morphology is of critically significance while an enhancement of photoinduced charge transfer plays an important role since the long charge-transfer states (CTS) impair exciton dissociation. One feasible approach is therefore to the construction of ternary blend OSCs by judiciously selecting a third component and tuning their molar ratio, which allows to synergistically optimize film morphology, enhance optical absorption and promote charge transport.[15,20–31]

In this work, we set out to investigate a benchmark binary blend NIR-NFA system based on a medium-E_g poly[4,8-bis(5-(2-ethylhexyl)thiophen-2-yl)benzo[1,2-b:4,5-b′]dithiophene-*co*-3-flfluorothieno[3,4-b]thiophene-2-carboxylate] (PTB7–Th) donor[32] (D) and IEICO–4F acceptor (A), which remains to suffer from both low J_{SC} and V_{OC}. Our studies confirm efficient charge transfer for both electrons and holes between PTB7–Th and IEICO–4F upon photoexcitation whereas the lifetimes of separated free charge carriers are quite short. This is presumably caused by the severe charge recombination occurring at the interfacial areas due to excellent miscibility between PTB7–Th and IEICO–4F in the blend film as well as small energetic gap between separated charge carriers. Therefore, by incorporation of either 3,9-bis(2-methylene-(3-(1,1-dicyanomethylene)-indanone)-5,5,11,11-tetrakis(4-hexylphenyl)-dithieno[2,3-d:2′,3′-d′]-s-indaceno[1,2-b:5,6-b′]dithiophene (ITIC)[32] or phenyl-C71-butyric acid methyl ester ($PC_{71}BM$)[15] as a mediator, in which ITIC has a good miscibility with PTB7–Th while $PC_{71}BM$ possesses excellent electron extraction capability, aiming to enhance interfacial charge separation. As a result, the optimal ternary OSCs based on PTB7–Th:IEICO–4F:ITIC (1:1.5:0.3, wt%) and PTB7–Th:IEICO–4F:$PC_{71}BM$ (1:1.5:0.1, wt%) blends deliver higher J_{SC} values of 21.9 and 25.4 mA cm^{-2}, respectively, yielding enhanced PCE of 10.2% and 10.6%, accordingly than that of the corresponding binary device (21.5 mA cm^{-2}, 9.3%). More importantly, this study reveals two major independent photophysical issues for efficient charge separation in conventional binary NIR-NFA OSCs, that is, long-lived interfacial CTS and short-path charge transportation with discontinued small-sized domains. An integration of appropriate third-component may tackle these issues yet what can resolve both deficiencies concurrently remains to be developed.

2. Results and Discussion

2.1. Optical Properties

The chemical structures and corresponding bandgaps (E_g) of PTB7–Th, IEICO–4F, ITIC, and $PC_{71}BM$ are displayed in **Figure 1**a,b, respectively. Both ITIC and $PC_{71}BM$ have a larger optical E_g than IEICO–4F, and their LUMO energy levels lie between those of PTB7–Th and IEICO–4F, which will improve V_{OC} in device. In addition, the formed cascade energy level alignment provides extra paths for electron transfer (ET) to strengthen exciton dissociation. Besides, the similar HOMO energy levels of ITIC and IEICO–4F will assist in hole transfer (HT) to PTB7–Th donor.

The representative optical absorption spectra of neat PTB7–Th, IEICO–4F, ITIC, and $PC_{71}BM$ films as well as their blend films are displayed in **Figure 2**a, respectively. ITIC shows strong light absorption that is overlapped with that of PTB7–Th. In the PTB7–Th:IEICO–4F:$PC_{71}BM$ blend, by contrast, neat $PC_{71}BM$ mainly absorbs light in 400–550 nm and complements well with both PTB7–Th and IEICO–4F to broaden light absorption. Both ternary blends however share one common feature, that is, a slight blue-shift of the absorption edge occurs when either ITIC or $PC_{71}BM$ is added, indicating that the third component might influence molecular packing in the blend film. Figure 2b shows the photoluminescence (PL) spectra of the binary and ternary blend films in comparison with the neat film of IEICO–4F. The PL spectra are acquired under photoexcitation at 808 nm where only IEICO–4F is excited. With the introduction of 20 wt% ITIC, the PL from IEICO–4F is quenched slightly in the IEICO–4F:ITIC blend film. This indicates that excitons in IEICO–4F could still be separated at the IEICO–4F/ITIC interfaces. This should be mainly attributed to the likely hole injection from IEICO–4F to ITIC despite slight

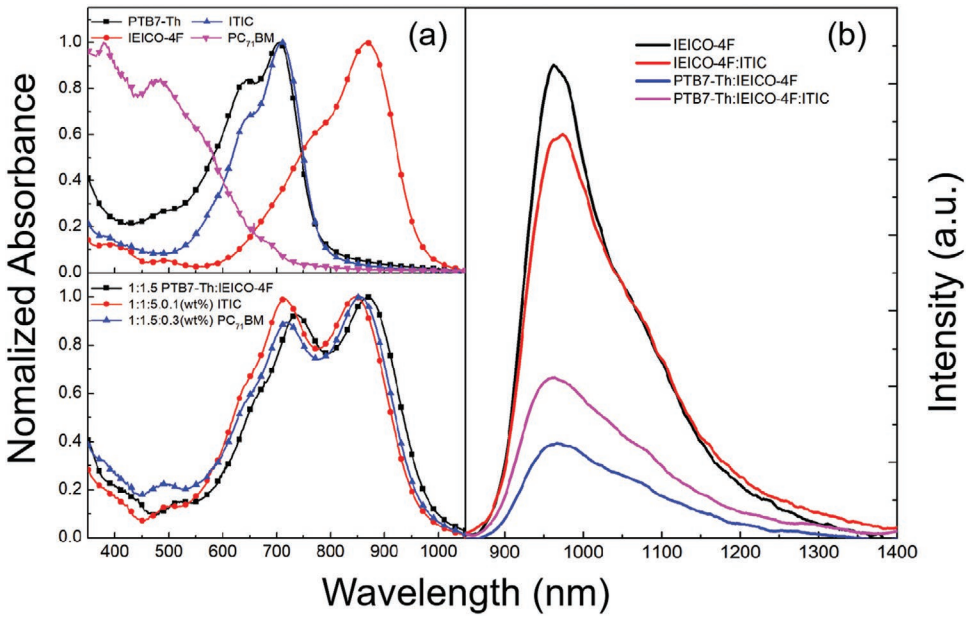

Figure 2. a) Optical absorption and b) photoluminescence (excited at 808 nm) spectra of PTB7–Th, IEICO–4F, ITIC, and $PC_{71}BM$ neat films along with their binary and ternary blend films.

lower HOMO level of ITIC as opposed to IEICO–4F according to the energy alignment in Figure 1b. However, such hole injection is not so efficient due to the insufficient driving force.[33] In the binary blend of PTB7–Th:IEICO–4F, the PL of IEICO–4F is remarkably quenched by PTB7–Th, suggestive of efficient hole transfer. When adding the optimal 20 wt% ITIC, such PL from IEICO–4F increases slightly, indicating that hole transfer from IEICO–4F to PTB7–Th is barely hindered by the existence of ITIC that acts as a potential barrier for hole injection. In the following studies, however, we found such retarded hole injection fails to influence the overall charge separation.

2.2. Molecular Packing

Next, grazing-incidence wide-angle X-ray scattering (GIWAXS) was employed to unveil the influences on molecular packing and orientation when adding the third component to the PTB7–Th:IEICO–4F blend. The obtained 2D GIWAXS patterns and the corresponding line-cuts are displayed in **Figure 3**a–e. It is obvious that the binary and ternary blend films exhibit a preferable face-on orientation ascribed to the (010) reflection of π-stack at the out-of-plane (OOP) direction.[34] As shown in Figure 3a, at the OOP direction, the binary blend film exhibits a moderate (010) π-stack at 1.76 $Å^{-1}$ and a relatively strong (100) lamellar reflection peak at 0.31 $Å^{-1}$, respectively. As shown in Figure 3b, the ternary PTB7–Th:IEICO–4F:ITIC blend film displays a stronger (010) reflection π-stack peak at 1.76 $Å^{-1}$ while a more distinct signal of the (100) lamellar reflection peak at 0.31 $Å^{-1}$ is observed than that in the binary blend. Then the coherent crystalline lengths (CCL) are calculated from the full width at half-maximum of OOP π-stack peaks via the Scherrer equation and then summarized in Table S1, Supporting Information. With the addition of ITIC, the CCL value in IEICO–4F increases from 2.66 to 2.79 nm while the modest changes of CCL in PTB7–Th are observed. This implies a better crystallinity of acceptor phases to promote the OOP-oriented charge transportation due to an incorporation of ITIC that is easier to crystalline than IEICO–4F as seen in Figure S1, Supporting Information. Besides, the neat ITIC film shows a strong lamellar ordering (Figure S1b, Supporting Information), which however vanish in the ternary blend film, indicating its excellent miscibility with PTB7–Th and IEICO–4F,[35] which could assist ITIC in tuning the nanoscale length of D:A phase segregation with uniform distribution. Likewise, the ternary PTB7–Th:IEICO–4F:$PC_{71}BM$ blend shows similar molecular packing motifs to those of the binary analogue, suggesting that the $PC_{71}BM$ addition has little effect on the packing structure in ternary blend film.

2.3. Film Morphology

Transmission electron microscope (TEM) and tapping-mode atomic force microscopy (AFM) were further employed to visualize the changes of film morphology from binary to ternary blends as compared in **Figure 4**. In the TEM images, the bright and dark regions represent donor-rich and acceptor-rich domains, respectively.[36] As shown in Figure 4a, the binary blend displays well-mixed phases, in which the IEICO–4F domains are distributed uniformly within the PTB7–Th regions without discernable segregation. Upon adding ITIC, the dark acceptor-rich domains are notably enlarged while still preserving an even phase-distribution (Figure 4b).[32] This could be caused by the deviation of the PTB7–Th miscibility with ITIC and IEICO–4f as shown in Figure S2, Supporting Information, which induce a preferential local crystallization during the film formation. Such enlarged acceptor domains provide continuous paths for charge transportation and hence could reduce carrier recombination which is also proved in the charge carrier dynamic studies in the following section. However, with the addition of $PC_{71}BM$,

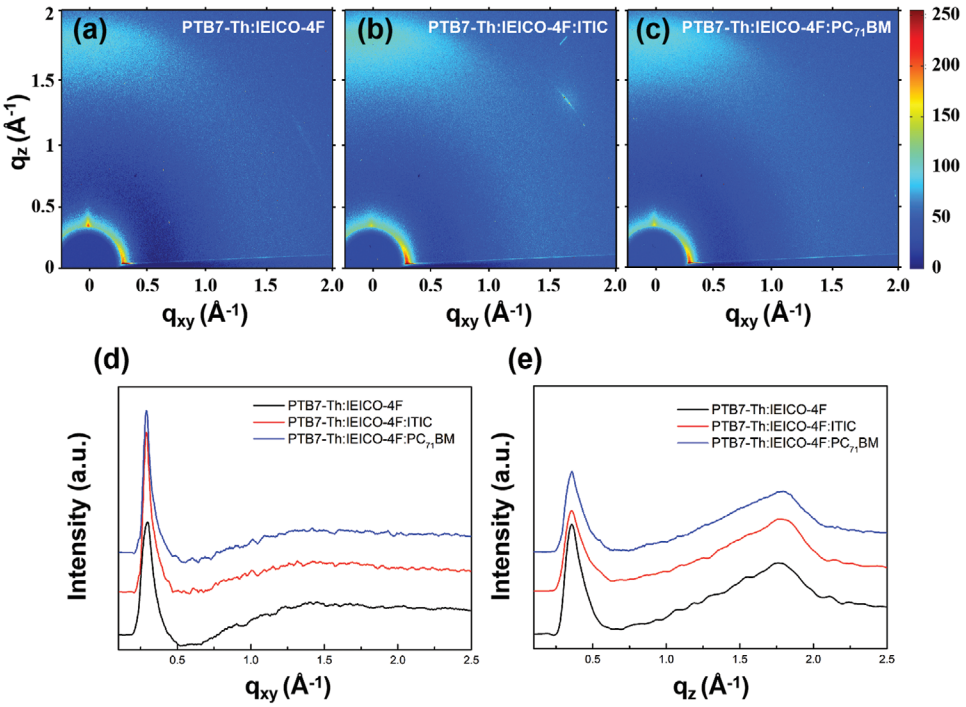

Figure 3. GIWAXS patterns of the a) binary and b,c) ternary blend films as well as the corresponding line-cut profiles along the d) in-plane and e) out-of-plane directions.

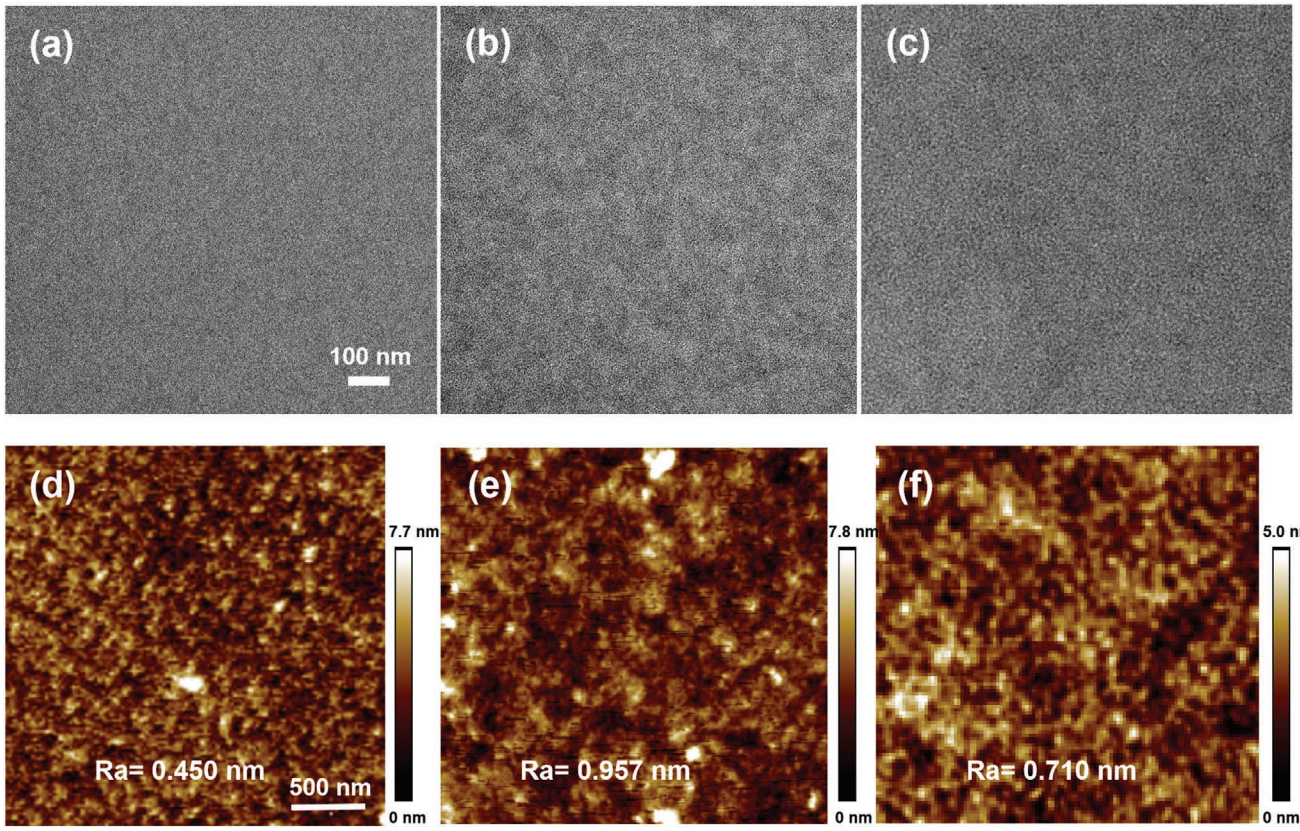

Figure 4. a–c) TEM and d–f) AFM images of binary and blend films: a,d) PTB7–Th:IEICO–4F, b,e) PTB7–Th:IEICO–4F:ITIC, and c,f) PTB7–Th:IEICO–4F:$PC_{71}BM$.

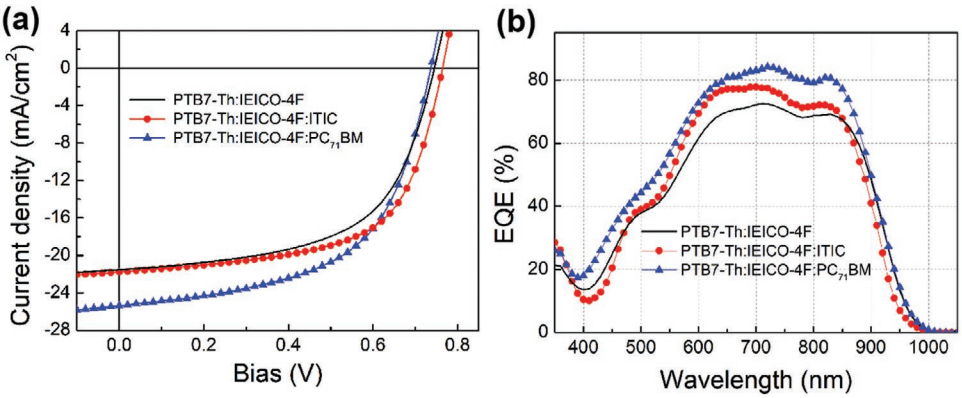

Figure 5. a) *J–V* curves and b) EQE curves of PTB7–Th:IEICO–4F based devices prepared with ITIC and $PC_{71}BM$, respectively.

the nanoscale fibrillar-like phase segregation of the light part is relatively clearer in Figure 4c, implying $PC_{71}BM$ very likely induces the PTB7–Th crystallization which could be related to the increased CCL of (100) lamellar reflection peak along the IP direction in GIWAXS data. In AFM images (Figure 4d–F), the root-mean-square roughness of binary and ternary blends are calculated to be 0.450, 0.957, and 0.710 nm, respectively. With the addition of ITIC, larger-sized domains are observed, which matches well with the corresponding TEM images.

2.4. Photovoltaic Cells

An inverted device structure of ITO/ZnO/active layer/MoO_X/Ag was employed to fabricate photovoltaic devices. **Figure 5**a and b show the light current density–voltage (*J–V*) curves and EQE spectra, respectively, and the corresponding photovoltaic parameters are listed in **Table 1**. The reference device based on the binary PTB7–Th:IEICO–4F blend shows an impressive PCE of 9.32%, which is well in accord with the literature values.[37,38] When adding the third component of ITIC or $PC_{71}BM$ with various contents, the optimal ternary devices exhibit the enhanced PCEs of 10.22% and 10.63%, respectively. The detailed performance parameters of ternary blend systems with different donor/acceptor ratios are shown in Tables S2 and S3, Supporting Information. By incorporating 20 wt% ITIC, both J_{SC} and V_{OC} are simultaneously improved to 21.87 mA cm^{-2} and 0.76 V, in which an increase of V_{OC} from 0.74–0.76 V could be ascribed to a higher LUMO energy level of ITIC than that of IEICO–4F. On the other hand, charge transfer could be more efficient in ternary blend to enhance J_{SC}. As such, an addition of 6 wt% $PC_{71}BM$ results in a significant increase of J_{SC} up to 25.38 mA cm^{-2}. Such an impressive photocurrent is mainly attributable to superior electron extraction ability of $PC_{71}BM$, which expedites photoinduced charge transfer. Additionally, light absorption of $PC_{71}BM$ around 350–500 nm could account for the increased EQE values around 500 nm.

We further studied device physics to acquire a better understanding of photon generation and charge recombination when comparing binary and ternary devices. First, charge carrier dynamics in device was investigated by measuring both the photocurrent density versus the effective applied voltage (J_{ph}–V_{eff}) characteristics and the dependence of J_{SC} on light illumination intensities (P_{light}). The obtained results are shown in Figure S4, Supporting Information, and summarized in Table S4, Supporting Information. Note that $J_{ph} = J_{light} - J_{dark}$ where J_{light} and J_{dark} refer to the current densities under illumination and in the dark, respectively, while $V_{eff} = V_0 - V_a$ where V_0 and V_a refers to the voltage when $J_{ph} = 0$ and the applied bias, respectively. At high V_{eff} (e.g., ≥3 V), all the photogenerated excitons are dissociated and collected by respective electrodes, and J_{sat} is only limited by the absorbed incident photons. Thus, J_{ph}/J_{sat} can be defined as the efficiency of charge extraction under short-circuit condition, which are calculated to be 91.9%, 94.9%, 94.3% in the optimal devices based on the blends of PTB7–Th:IEICO–4F, PTB7–Th:IEICO–4F:ITIC, and PTB7–Th:IEICO–4F:$PC_{71}BM$ with the component ratio of 1:1.5, 1:1.5:0.3, and 1:1.5:0.1 (wt%), respectively. For the sake of brevity in the following discussion, the above blend films of are denoted as I, II, and III, respectively. These results indicate

Table 1. Summary of photovoltaic parameters of the binary and ternary devices under simulated light irradiation of 100 mW cm^{-2}.

Blend	Component weight ratio	J_{SC} [mA cm^{-2}]	V_{OC} [V]	FF [%]	PCE [%]
PTB7–Th: IEICO–4F	1:1.5	20.62 ± 1.18 (21.52a)/19.54b))	0.74 ± 0.01 (0.74)	58.55 ± 0.02 (58.52)	8.96 ± 0.23 (9.32)
PTB7–Th: IEICO–4F:ITIC	1:1.5:0.3	22.27 ± 0.68 (21.87a)/20.31b))	0.76 ± 0.02 (0.76)	60.13 ± 0.02 (61.79)	10.05 ± 0.25 (10.22)
PTB7–Th: IEICO–4F:$PC_{71}BM$	1:1.5:0.1	23.63 ± 2.06 (25.38[a])/23.13[b])	0.74 ± 0.01 (0.74)	58.00 ± 0.03 (56.59)	10.15 ± 0.41 (10.63)

[a]The average values of photovoltaic parameters were obtained from at least 5 devices and the values in parentheses are the highest values; [b]The J_{SC} values were calculated from the EQE results.

that ternary devices with 20 wt% ITIC or 6 wt% $PC_{71}BM$ exhibit more efficient charge generation and dissociation than the binary devices. Furthermore, the dependence of J_{SC} on P_{light} was studied to probe the carrier recombination behaviours of the devices and then fitted with the equation of $J_{SC} \propto (P_{light})^{\alpha}$.[S3] The obtained α values are 0.985, 0.990, and 1.02 in devices of I, II, and III, respectively. These results show that the addition of 20 wt% ITIC could suppress the bimolecular recombination. In contrast, such a recombination in $PC_{71}BM$ based devices cannot be neglected. This is also reflected in their relatively lower FF as FF is strongly correlated with the relative rates of charge recombination and extraction of free charges.[39,40] The plausible reason is that the $PC_{71}BM$ addition may break the continuity of IEICO–4F phases to generate additional grain boundaries, as evidenced by an increased surface roughness from the AFM measurement in Figure 4f. The trap states induced at the grain boundary will attract one species of charge carriers—either electrons or holes. The ensuing accumulation of spatial charges provides more chances for local carrier recombination.

The charge mobilities were then measured by the space charge-limited current (SCLC) measurements, in which hole-only device of ITO/PEDOT:PSS/active layer/Au and electron-only device of ITO/ZnO/active layer/Ca/Al were fabricated to calculate electron and hole mobilities in devices, respectively. Dark *J*–*V* curves of the devices are fitted to the SCLC model, as shown in Figure S5, Supporting Information. The calculated hole (μ_h) and electron (μ_e) mobilities along with μ_h/μ_e values are summarized in Table S4, Supporting Information. The μ_e of device II (4.15×10^{-5} cm^2 V^{-1} s^{-1}) is larger than that of device I (3.37×10^{-5} cm^2 V^{-1} s^{-1}). This could be ascribed to the appropriate phase-separated domain size as induced by IEICO–4F with improved crystallinity.[41] On the other hand, the μ_e of device III increases subtly to 4.01×10^{-5} cm^2 V^{-1} s^{-1} with minor $PC_{71}BM$ incorporated.

2.5. Photodetectors

Given remarkably high photocurrents obtained in the above NIR-NFA OSCs, we further investigated the organic photodetector (OPD) performance based on the same above OSC device structure. The ternary OPD device based on PTB7–Th:IEICO–4F:ITIC (**Figure 6**) shows relatively higher light currents than binary device (Figure S6, Supporting Information). As shown in Figure 6a, the ternary OPD device shows an ultra-low dark current density of 5.33×10^{-11} A cm^{-2} at 0 V bias, which is much lower than many of the previously reported OPDs[42] and also critically important to specific detectivity (*D*). Spectral responsivity (*R*) is another key parameter of photodetectors, for which we adopt the equation of $R = (I_{ph}-I_d)/P$ where *P* is the incident light intensity, I_{ph} and I_d are the dark and light currents.[43] Our OPD devices achieve a high *R* of 0.52 A W^{-1} under an illumination of 845 nm monochromatic infrared light with an intensity of 60 μW cm^{-2}, which shows a promising NIR sensitivity. Thus, the specific detectivity (*D*) is determined to be 1.25×10^{14} Jones by using the equation of $D = R/(2qJ_d)^{1/2}$.[42] Note that this outstanding *D* value is among the best reported self-powered photodetectors. By characterizing the current as a function of time when the light was switched on and off every 10 s, the ON/OFF ratio of the OPD device maintains a high value of 10^6 with excellent reproducibility as shown in Figure 6b.[44]

2.6. Photophysics

In order to obtain the detailed charge carrier dynamics to rationalize the device performance, we conducted the transient absorption (TA) measurement of the samples—PTB7–Th:IEICO–4F (I), PTB7–Th:IEICO–4F:ITIC (II), and PTB7–Th:IEICO–4F:$PC_{71}BM$ (III)—as illustrated in **Figure 7**. Figure 7A shows the TA spectrogram of I excited at 570 nm. Thanks to the larger excitation phonon energy compared with the optical E_gs of the donor and acceptor, both components would be excited. Two negative bands at 720 and 840 nm can be attributed to the ground state bleach (GSB) of PTB7–Th and IEICO–4F, respectively, corresponding to the steady state absorption bands in Figure 2a. In II with 20 wt% ITIC shown as ITIC0.3 in Figure 7, the TA spectra with similar bleach bands are found as shown in Figure 7B, indicating ITIC plays a minor role in light absorption. Next, we identify charge transfer between the donor and acceptors by analyzing the TA kinetics at characteristic bleach bands, which is summarized in Figure 7C at the maximum of the GSB for PTB7–Th (719 nm) in neat PTB7–Th, binary and ITIC-added ternary films, which reflect the depopulation dynamics of the excited electrons and holes at the HOMO and LUMO energy levels of PTB7–Th in those samples after light excitation. Compared to in neat PTB7–Th (black line), the TA kinetics in the other two

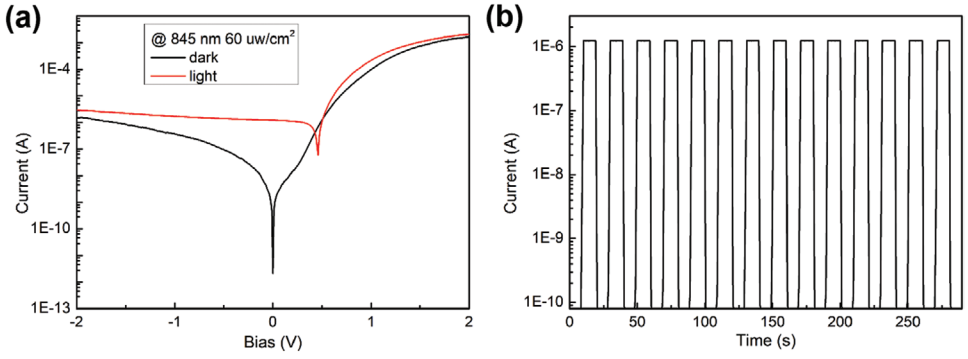

Figure 6. a) *J*–*V* curves and b) transient photocurrent of vertical-structured OPDs with PTB7–Th:IEICO–4F:ITIC blends.

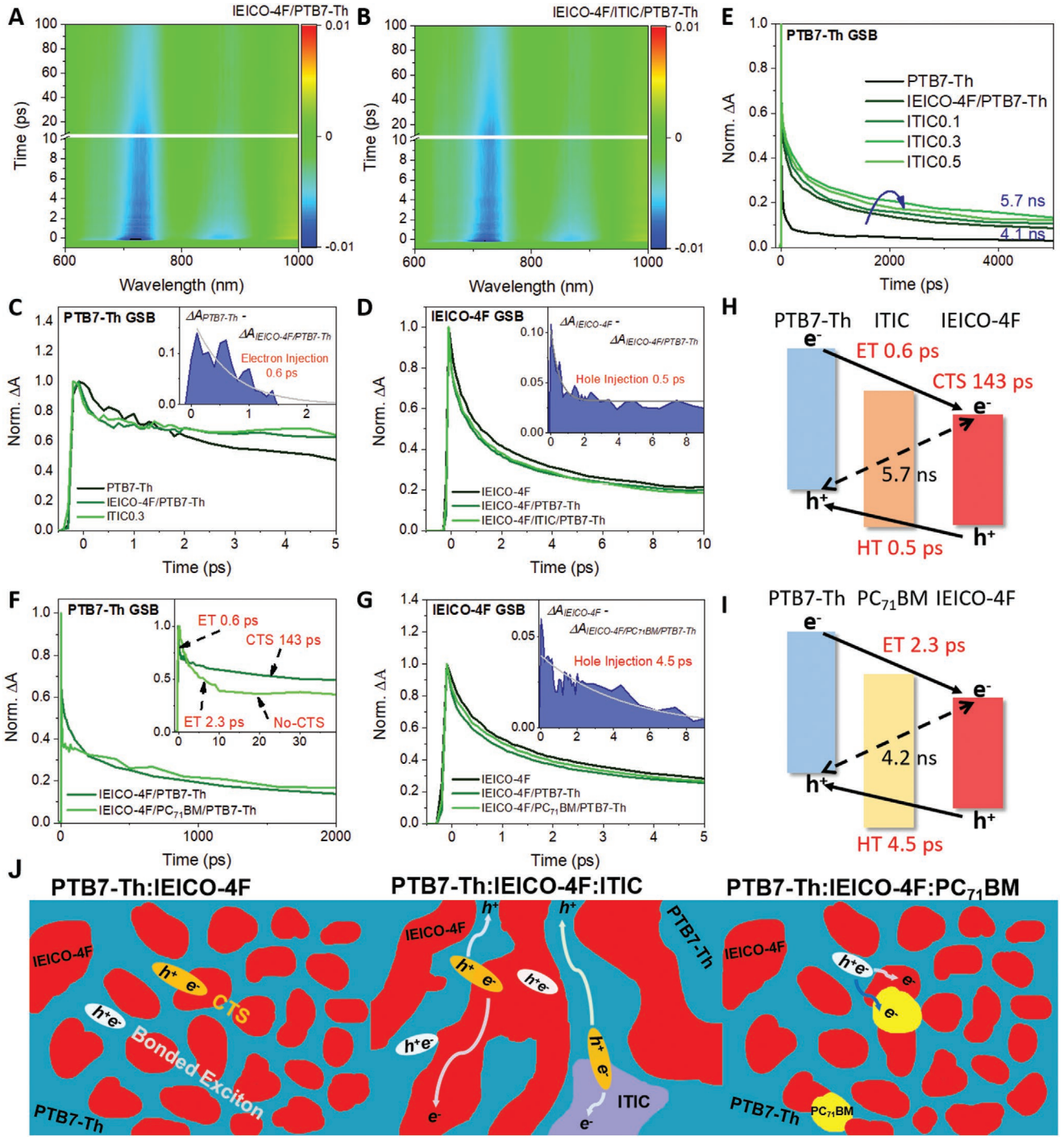

Figure 7. TA spectra of A) I and B) II with 570 nm excitation. C) TA kinetics at PTB7–Th GSB (probed at 719 nm and excited at 570 nm) of PTB7–Th, I, and II with the inset showing the differential kinetics between PTB7–Th and I. D) TA kinetics at IEICO–4F GSB (probe at 868 nm, excited at 840 nm) of PTB7–Th, I, and II with the inset showing the differential kinetics between PTB7–Th and I. E) TA kinetics at PTB7–Th GSB (probe at 719 nm, excited at 570 nm) of PTB7–Th, I, and II with various ITIC contents. F) TA kinetics at PTB7–Th GSB (probe at 719 nm, excited at 570 nm) of I and III with the inset showing the early time scale range. G) TA kinetics at IEICO–4F GSB (probe at 868 nm, excited at 840 nm) of IEICO–4F, I, and III with the inset showing the differential kinetics between IEICO–4F and III. Schematics of all the charge carrier transfer processes in H) II and I) III and J) charge transportation pathways in the blend films.

samples decay first faster up to 2 ps and then become slower at longer time delay. The initial fastened decay indicates the existence of extra excited state depopulation pathway, that is, electron transfer from PTB7–Th to IEICO–4F as it is energetically favorable. We can extract the electron injection time to be 0.6 ps by exponentially fitting the differential decay between

the neat PTB7–Th and binary film as shown in the inset of Figure 7C. The slower decays after 2 ps in both I and II indicate a delayed excited state depopulation in PTB7–Th despite an initial ultrafast electron injection. In addition, the singular value decomposition analysis of the TA spectrum of binary film clearly extracts one spectral component featured with GSB bands that blue-shift the GSB band edge of both donor and acceptor as illustrated in Figure S7, Supporting Information. It is a fingerprint of the formation of CTS where the injection electrons in acceptors are still bounded with the residual holes in donor by an extra coulombic energy, which has been observed in our previous researches in both OPV and quantum dot systems.[15,45] More importantly, we found almost the same PTB7–Th GSB decay kinetics at the early time scale for both I and II indicating ITIC would not affect electron injection in this scenario. On the other hand, the hole injection dynamics from IEICO–4F to PTB7–Th can be extracted from the TA kinetics of the IEICO–4F GSB (850 nm) when 840 nm excitation is used where only the IEICO–4F can be excited as shown in Figure 7D. The faster TA decays of binary and ternary films at this wavelength compared with neat IEICO–4F characterize the hole injection channel between the donor and the acceptor. Likewise, the hole injection can be calculated to be 0.5 ps from the differential decay between the neat IEICO–4F and binary films as indicated in inset of Figure 7D. Similar to electron injection, the influence of ITIC on hole injection is also negligible with the similar TA decays at IEICO–4F GSB. The negligible effect of ITIC on both electron and hole injection between PTB7–Th and IEICO–4F can be well expected as both its HOMO and LUMO energy levels locate in-between or close to PTB7–Th and IEICO–4F where no pronounced potential barrier can be imposed at the D/A interface. However, significant difference after ITIC addition is observed in the PTB7–Th GSB at long time delay as seen from 200 ps to 5 ns in Figure 7E. Such time scale is much longer than both the electron/hole injection time and the electron–hole recombination time in both donor and acceptors as seen from the TA decay of neat PTB7–Th GSB in Figure 7E. Therefore, it only represents the geminate recombination between the separated electrons and holes. The slower decays of II with various ITIC contents relative to I manifest the deterred interfacial geminate recombination. In addition, we observe the slowest recombination time of 5.7 ns in the optimal sample with 20 wt% ITIC addition, which is consistent with the best device performance as mentioned above.

On the contrary to ITIC, when $PC_{71}BM$ is added, the electron and hole injection between the PTB7–Th and IEICO–4F would be drastically modified as illustrated in Figure 7F,G. Figure 7F shows the PTB7–Th GSB with 570 nm excitation of I and III The TA decay of the III can be well-fitted by only two exponential components with lifetime of 2.3 ps and 4.2 ns, respectively, where no intermediate component related to the CTS dissociation can be found as seen in inset of Figure 7F. Such phenomenon also emerges in the OSC system including ITIC in our previous report.[15] We believe it results from the relatively high dielectric constant and high conductivity of $PC_{71}BM$ that effectively screens the columbic interaction between the separated charges at the D/A interfaces. On the other hand, the hole injection from IEICO–4F to PTB7–Th is slighted decelerated to 4.5 ps as evaluated from the IEICO–4F GSB comparison in Figure 7G. This can be attributed to an extra energy barrier for the HT created by $PC_{71}BM$ due to its lower HOMO energy level than both PTB7–Th and IEICO–4F as shown in Figure 1b. Therefore, the improved photovoltaic performance with $PC_{71}BM$ addition should be mainly contributed by the enhanced ET at the D/A interfaces.

In general, the perfect phase miscibility and energy level alignment between PTB7–Th and IEICO–4F guarantee the efficient charge separation at the D/A interfaces. To the best of our knowledge, the observed both 0.6 ps ET and 0.5 ps HT time are among the fastest in reported NFA-OSCs.[15,46] However, as schematically illustrated in Figure 7J, such good miscibility would probably reduce the individual domain size of either donor or acceptor, and consequently restrict the charge transportation channels. The addition of ITIC can modulate film morphology to create elongated continuous donor or acceptor domains for charge carrier transportation as shown in Figure 7H, while the addition of $PC_{71}BM$ plays an entirely different role in optimizing the interfacial charge transfer dynamics. As the CTS can be diminished accordingly via $PC_{71}BM$, the driving force required for the charge transfer can be much less, which offers large potential to reduce the V_{OC} loss by band energy engineering in the future for such system as shown in Figure 7I.

From the above analysis, it is evident that the long-lived CTS and the lack of long-range charge transportation pathway serve as two main photo-physical challenges constraining the device performance in binary NIR-NFA OSCs. In addition, we experimentally proved that when the above two ternary additions were exploited jointly, thereby forming a quaternary blend of PTB7–Th:IEICO–4F:ITIC:$PC_{71}BM$, the device however performed worse. This may suggest plausible complex interaction between these two third-components. On the other hand, two critical factors that restrict charge separation are believed to be independent in NIR-NFA OSCs that should be tackled in parallel to ultimately enhance device performance. A desirable scenario is to develop such a third-component that integrates the relatively high dielectric constant to diminish the interfacial CTS and the capability to tune D/A phase segregation for larger domain sizes.

3. Conclusions

In conclusion, we have revealed two critical issues of interfacial charge separation in the paradigm NIR-NFA OSCs based on PTB7–Th donor and IEICO–4F acceptor and then resolve them by inclusion of an appropriate third-component while unravelling their individual dynamic role in the system. Firstly, TA studies verify efficient charge transfer between PTB7–Th and IEICO–4F accompanied by geminate recombination of the photo-excited charge carriers. Then, the two hurdles restricting charge separation are unveiled. One is the discontinuity of connecting individual phases in the blend correlated to the good D:A miscibility while the other is the long-lived CTS retarding interfacial dissociation, which relates to the conductivity of component materials. Third,

both issues are resolved accordingly by incorporation of third-component NFA (ITIC) or FA ($PC_{71}BM$) with various molar ratios yet in different dynamic mechanisms. ITIC molecules are distributed uniformly in the blends which favors appropriate enlargement of either D or A domains to create more continuous paths for charge carrier transportation, as evidenced by a clear prolonged lifetime of separated charge carriers. On the other hand, an inclusion of $PC_{71}BM$ diminishes CTS and enhances electron transfer at the D/A interfaces. As a result, the optimal ternary OSCs comprising 0.3 wt% ITIC and 0.1 wt% $PC_{71}BM$ in the blend deliver higher J_{SC} values of 21.9 (along with improved V_{OC}) and 25.4 mA cm^{-2}, enhanced PCEs of 10.2% and 10.6% without any additive or annealing treatment. Based on the same devices, a self-powered photodetector with high NIR sensitivity is also demonstrated, showing dual-functionalities in organic optoelectronics. A critical finding of this work is that we identified two photophysical limitations in paradigm binary NIR-NFA OSCs that would be universal in most of such systems considering similar physical and chemical characteristics of NIR-NFA materials. Intriguingly, those two constraints are found to impact independently on NIR-NFA OSCs and we therefore suggest that a desirable third-component would be to integrate the function of mediating phase miscibility and extracting electron efficiently, which tackles both challenges simultaneously and appears a key to break the performance limit of NIR-NFA OSCs.

Supporting Information

Supporting Information is available from the Wiley Online Library or from the author.

Acknowledgements

The support of National Natural Science Foundation of China (NSFC) under grant No. 51473036 (Z.L.), NSFC-The Swedish Foundation for International Cooperation in Research and Higher Education (STINT) No. 5191101797 (Z.L.), Danish Council for Independent Research No. 7026-0037B, and Swedish Research Council No. 2017–05337 (K.Z.) were acknowledged. The authors thank beamline BL14B1 (Shanghai Synchrotron Radiation Facility) for providing the beam time and helps during experiments. W.L. is grateful for the support of China Scholarship Council (CSC) under grant No. 201806460021.

Conflict of Interest

The authors declare no conflict of interest.

Keywords

charge and energy transfer, charge recombination, near-infrared, nonfullerene acceptors, organic solar cells

Received: February 19, 2020
Revised: April 9, 2020
Published online: May 28, 2020

[1] J. Zhang, H. S. Tan, X. Guo, A. Facchetti, H. Yan, *Nat. Energy* **2018**, *3*, 720.
[2] G. Li, W.-H. Chang, Y. Yang, *Nat. Rev. Mater.* **2017**, *2*, 17043.
[3] L. Lu, T. Zheng, Q. Wu, A. M. Schneider, D. Zhao, L. Yu, *Chem. Rev.* **2015**, *115*, 12666.
[4] W. Huang, Z. Jiang, K. Fukuda, X. Jiao, C. R. McNeill, T. Yokota, T. Someya, *Joule* **2020**, *4*, 128.
[5] C. Yan, S. Barlow, Z. Wang, H. Yan, A. K. Y. Jen, S. R. Marder, X. Zhan, *Nat. Rev. Mater.* **2018**, *3*, 18003.
[6] J. Hou, O. Inganas, R. H. Friend, F. Gao, *Nat. Mater.* **2018**, *17*, 119.
[7] P. Cheng, G. Li, X. Zhan, Y. Yang, *Nat. Photonics* **2018**, *12*, 131.
[8] H. Yao, Y. Chen, Y. Qin, R. Yu, Y. Cui, B. Yang, S. Li, K. Zhang, J. Hou, *Adv. Mater.* **2016**, *28*, 8283.
[9] Y. Lin, J. Wang, Z. G. Zhang, H. Bai, Y. Li, D. Zhu, X. Zhan, *Adv. Mater.* **2015**, *27*, 1170.
[10] D. Su, M.-A. Pan, Z. Liu, T.-K. Lau, X. Li, F. Shen, S. Huo, X. Lu, A. Xu, H. Yan, C. Zhan, *Chem. Mater.* **2019**, *31*, 8908.
[11] T. Li, S. Dai, Z. Ke, L. Yang, J. Wang, C. Yan, W. Ma, X. Zhan, *Adv. Mater.* **2018**, *30*, 1705969.
[12] P. Cheng, J. Wang, Q. Zhang, W. Huang, J. Zhu, R. Wang, S. Y. Chang, P. Sun, L. Meng, H. Zhao, H. W. Cheng, T. Huang, Y. Liu, C. Wang, C. Zhu, W. You, X. Zhan, Y. Yang, *Adv. Mater.* **2018**, *30*, 1801501.
[13] D. Baran, T. Kirchartz, S. Wheeler, S. Dimitrov, M. Abdelsamie, J. Gorman, R. S. Ashraf, S. Holliday, A. Wadsworth, N. Gasparini, P. Kaienburg, H. Yan, A. Amassian, C. J. Brabec, J. R. Durrant, I. McCulloch, *Energy Environ. Sci.* **2016**, *9*, 3783.
[14] W. Zhao, D. Qian, S. Zhang, S. Li, O. Inganas, F. Gao, J. Hou, *Adv. Mater.* **2016**, *28*, 4734.
[15] X. Liu, Y. Yan, A. Honarfar, Y. Yao, K. Zheng, Z. Liang, *Adv. Sci.* **2019**, *6*, 1802103.
[16] H. Yao, L. Ye, J. Hou, B. Jang, G. Han, Y. Cui, G. M. Su, C. Wang, B. Gao, R. Yu, H. Zhang, Y. Yi, H. Y. Woo, H. Ade, J. Hou, *Adv. Mater.* **2017**, *29*, 1700254.
[17] H. Huang, Q. Guo, S. Feng, C. Zhang, Z. Bi, W. Xue, J. Yang, J. Song, C. Li, X. Xu, Z. Tang, W. Ma, Z. Bo, *Nat. Commun.* **2019**, *10*, 3038.
[18] J. Wang, S. Xie, D. Zhang, R. Wang, Z. Zheng, H. Zhou, Y. Zhang, *J. Mater. Chem. A* **2018**, *6*, 19934.
[19] H. Yao, Y. Cui, R. Yu, B. Gao, H. Zhang, J. Hou, *Angew. Chem., Int. Ed.* **2017**, *56*, 3045.
[20] M. Pan, T. Lau, Y. Tang, Y. Wu, T. Liu, K. Li, M. Chen, X. Lu, W. Ma, C. Zhan, *J. Mater. Chem. A* **2019**, *7*, 20713.
[21] R. Yu, S. Zhang, H. Yao, B. Guo, S. Li, H. Zhang, M. Zhang, J. Hou, *Adv. Mater.* **2017**, *29*, 1700437.
[22] J.-H. Kim, C. Schaefer, T. Ma, J. Zhao, J. Turner, M. Ghasemi, I. Constantinou, F. So, H. Yan, A. Gadisa, H. Ade, *Adv. Energy Mater.* **2019**, *9*, 1802293.
[23] N. Felekidis, E. Wang, M. Kemerink, *Energy Environ. Sci.* **2016**, *9*, 257.
[24] W. Tress, B. Beyer, N. A. Astani, F. Gao, S. Meloni, U. Rothlisberger, *J. Phys. Chem. Lett.* **2016**, *7*, 3936.
[25] D. Baran, R. S. Ashraf, D. A. Hanifi, M. Abdelsamie, N. Gasparini, J. A. Rohr, S. Holliday, A. Wadsworth, S. Lockett, M. Neophytou, C. J. Emmott, J. Nelson, C. J. Brabec, A. Amassian, A. Salleo, T. Kirchartz, J. R. Durrant, I. McCulloch, *Nat. Mater.* **2017**, *16*, 363.
[26] N. Gasparini, A. Salleo, I. McCulloch, D. Baran, *Nat. Rev. Mater.* **2019**, *4*, 229.
[27] Q. Zhao, Z. Xiao, J. Qu, L. Liu, H. Richter, W. Chen, L. Han, M. Wang, J. Zheng, Z. Xie, L. Ding, F. He, *ACS Energy Lett.* **2019**, *4*, 1106.
[28] V. Tamilavan, Y. Liu, J. Lee, I. Shin, Y. K. Jung, B. R. Lee, J. H. Jeong, S. H. Park, *ACS Appl. Energy Mater.* **2019**, *2*, 4284.
[29] M. Nam, J. Yoo, Y. Park, H. Y. Noh, Y. Park, J. Cho, J.-A. Kim, J. Kim, H. H. Lee, R. Chang, D.-H. Ko, *J. Mater. Chem. A* **2019**, *7*, 9698.

[30] W. T. Hadmojo, F. T. A. Wibowo, W. Lee, H. K. Jang, Y. Kim, S. Sinaga, M. Park, S. Y. Ju, D. Y. Ryu, I. H. Jung, S. Y. Jang, *Adv. Funct. Mater.* **2019**, *29*, 1808731.
[31] N. Gasparini, S. Kahmann, M. Salvador, J. D. Perea, A. Sperlich, A. Baumann, N. Li, S. Rechberger, E. Spiecker, V. Dyakonov, G. Portale, M. A. Loi, C. J. Brabec, T. Ameri, *Adv. Energy Mater.* **2019**, *9*, 1803394.
[32] X. Liu, J. Wang, J. Peng, Z. Liang, *Macromolecules* **2017**, *50*, 6954.
[33] Q. Li, Y. Sun, X. Xue, S. Yue, K. Liu, M. Azam, C. Yang, Z. Wang, F. Tan, Y. Chen, *ACS Appl. Mater. Interfaces* **2019**, *11*, 3299.
[34] W. T. Hadmojo, F. T. A. Wibowo, W. Lee, H.-K. Jang, Y. Kim, S. Sinaga, M. Park, S.-Y. Ju, D. Y. Ryu, I. H. Jung, S.-Y. Jang, *Adv. Funct. Mater.* **2019**, *29*, 1808731.
[35] X. Yang, J. K. J. van Duren, R. A. J. Janssen, M. A. J. Michels, J. Loos, *Macromolecules* **2004**, *37*, 2151.
[36] X. Song, N. Gasparini, L. Ye, H. Yao, J. Hou, H. Ade, D. Baran, *ACS Energy Lett.* **2018**, *3*, 669.
[37] H. W. Cheng, H. Zhang, Y. C. Lin, N. Z. She, R. Wang, C. H. Chen, J. Yuan, C. S. Tsao, A. Yabushita, Y. Zou, F. Gao, P. Cheng, K. H. Wei, Y. Yang, *Nano Lett.* **2019**, *19*, 5053.
[38] Z. Zheng, R. Wang, H. Yao, S. Xie, Y. Zhang, J. Hou, H. Zhou, Z. Tang, *Nano Energy* **2018**, *50*, 169.
[39] N. Gasparini, X. Jiao, T. Heumueller, D. Baran, G. J. Matt, S. Fladischer, E. Spiecker, H. Ade, C. J. Brabec, T. Ameri, *Nat. Energy* **2016**, *1*, 16118.
[40] D. Bartesaghi, C. P. Idel, J. Kniepert, S. Roland, M. Turbiez, D. Neher, L. J. Koster, *Nat. Commun.* **2015**, *6*, 7083.
[41] H. Wu, B. Zhao, H. Zhao, L. Wang, W. Wang, Z. Cong, J. Liu, W. Ma, C. Gao, *ACS Appl. Mater. Interfaces* **2020**, *12*, 789.
[42] J. Huang, J. Lee, J. Vollbrecht, V. V. Brus, A. L. Dixon, D. X. Cao, Z. Zhu, Z. Du, H. Wang, K. Cho, G. C. Bazan, T. Q. Nguyen, *Adv. Mater.* **2019**, *31*, 1906027.
[43] W. Li, Y. Xu, X. Meng, Z. Xiao, R. Li, L. Jiang, L. Cui, M. Zheng, C. Liu, L. Ding, Q. Lin, *Adv. Funct. Mater.* **2019**, *29*, 1808948.
[44] Z. Liu, T.-K. Lau, G. Zhou, S. Li, J. Ren, S. K. Das, R. Xia, G. Wu, H. Zhu, X. Lu, H.-L. Yip, H. Chen, C. Li, *Nano Energy* **2019**, *63*, 103807.
[45] K. Zidek, K. Zheng, C. S. PonsecaJr., M. E. Messing, L. R. Wallenberg, P. Chabera, M. Abdellah, V. Sundstrom, T. Pullerits, *J. Am. Chem. Soc.* **2012**, *134*, 12110.
[46] H. Bin, L. Gao, Z.-G. Zhang, Y. Yang, Y. Zhang, C. Zhang, S. Chen, L. Xue, C. Yang, M. Xiao, *Nat. Commun.* **2016**, *7*, 13651.